Applied Catalysis B: Environmental 332 (2023) 122743

Contents lists available at ScienceDirect

Applied Catalysis B: Environmental

journal homepage: www.elsevier.com/locate/apcatb

Unravelling the role of metal-metal oxide interfaces of $Cu/ZnO/ZrO_2/Al_2O_3$ catalyst for methanol synthesis from CO_2: Insights from experiments and DFT-based microkinetic modeling

Balaji C. Dharmalingam [a,1], Ajay Koushik V [a,1], Mauro Mureddu [b], Luciano Atzori [b,c], Sarah Lai [b], Alberto Pettinau [b], Niket S. Kaisare [a,*], Preeti Aghalayam [a,*], Jithin John Varghese [a,*]

[a] Department of Chemical Engineering, Indian Institute of Technology Madras, Chennai 600036, India
[b] Sotacarbo S.p.A., Grande Miniera di Serbariu, Carbonia 09013, Italy
[c] Department of Chemical and Geological Sciences, University of Cagliari, Monserrato 09042, Italy

ARTICLE INFO

Keywords:
DFT
Microkinetic modeling
Methanol production
CO_2 hydrogenation
Copper-Zinc-Zirconia
Multiscale modeling

ABSTRACT

$Cu/ZnO/ZrO_2/Al_2O_3$ catalysts are widely explored for CO_2 conversion to methanol due to their higher activity and stability. However, mechanistic understanding of the performance of such catalysts is lacking due to ambiguity on the actual active sites. This study focuses on unraveling the nature of different interfaces on $Cu/ZnO/ZrO_2/Al_2O_3$ catalyst by coupling experiments, Density Functional Theory (DFT) simulations and a DFT-based reactor scale multi-site microkinetic model. Although DFT calculations suggested the ZrO_2/Cu interface to be the CO_2 adsorption site, the validated microkinetic model predicted the ZnO/Cu interface to be the crucial reaction center. Reaction pathway analysis showed that methanol is produced through the formate pathway near the reactor entrance, whereas, the carboxyl pathway dominates in the latter zones, emphasizing the occurrence of both CO_2 and CO hydrogenation. This deeper understanding of the reaction behavior of such multicomponent catalysts will aid in designing better catalysts and optimizing reaction conditions and systems.

1. Introduction

Carbon dioxide is one of the important greenhouse gases released into the earth's atmosphere, raising global temperature, which is increasing at an average rate of 0.18 °C per decade since 1981 [1]. There is a need to cut down the anthropogenic CO_2 emission and sequester or utilize CO_2 to limit the temperature rise to 1.5 °C above the pre-industrial levels [2]. Carbon Capture Utilization and Storage (CCUS) is proven to mitigate the impact of CO_2 emissions [3,4]. Among the available routes for CO_2 mitigation, utilizing CO_2 has gained attention, as CO_2 can act as a potential feedstock for producing value-added chemicals [4]. One such way of the utilization of CO_2 as a feedstock is thermocatalytic reduction using H_2 from sources such as solar, wind, or other renewables to produce methanol, methane, syngas, and other organic compounds [5,6]. Methanol production from CO_2 hydrogenation has gained importance because it is cleaner compared to the other fuels and is a potential hydrogen carrier. It can also be used as a feedstock to produce other commodity chemicals such as acetic acid, dimethyl ether, and higher hydrocarbons.

Catalysts play a critical role in lowering the energy requirements for the reduction reaction and in the selective production of methanol. Typical industrial production of methanol is carried out from CO-rich syngas at temperatures of 200–300 °C and high pressure of 50–100 bar in the presence of $Cu/ZnO/Al_2O_3$ catalysts [7]. However, this catalyst is unstable for CO_2-rich feeds due to water formation from CO_2 hydrogenation [8]. Addition of promoters such as ZrO_2 [9], CeO_2 [10,11] or both [12,13] to the $Cu/ZnO/Al_2O_3$ catalyst to improve its performance for CO_2-rich feeds were explored. Numerous investigations have demonstrated the superior performance of the ternary $Cu/ZnO/ZrO_2$ [14–22] catalyst towards enhanced methanol yield. The promotional effect of Zr in the $Cu/ZnO/Al_2O_3$ catalysts has been attributed to multiple reasons in the literature, such as increasing catalyst stability and performance by inhibiting water poisoning [19], enhancing CO_2 sorption capacity of the catalyst and hence methanol selectivity [21,23], and direct participation of Zr (or an appropriate interface involving Zr) in the reaction mechanism, thereby directing the selective formation of

* Corresponding authors.
E-mail addresses: nkaisare@iitm.ac.in (N.S. Kaisare), preeti@iitm.ac.in (P. Aghalayam), jithinjv@iitm.ac.in (J.J. Varghese).
[1] These authors contributed equally to this work and should be considered co-first authors.

https://doi.org/10.1016/j.apcatb.2023.122743
Received 14 December 2022; Received in revised form 20 March 2023; Accepted 5 April 2023
Available online 6 April 2023
0926-3373/

methanol [24,25]. Some other investigations however point to an indirect role of Zr in catalytic performance, for example by enriching the physicochemical properties of the catalyst such as Cu dispersion (D_{Cu}) and Cu surface area (S_{Cu}) which also enhance CO_2 conversion [26,27]. Consequently, a $Cu/ZnO/ZrO_2/Al_2O_3$ catalyst is investigated for the CO_2 to methanol reaction. Specifically, this work focuses on unraveling the role of the ZnO and ZrO_2 components and the interfaces of this multi-component catalyst.

Density Functional Theory (DFT) calculations are handy in understanding detailed catalytic reaction mechanisms, and exploring the role of interfacial interaction of binary catalysts (Cu/ZnO [28,29], Cu/ZrO_2 [25,30,31] and ZnO/ZrO_2 [32]). A few studies on the binary catalysts emphasized the importance of metal/metal oxide interface for CO_2 adsorption [33,34]. However, limited studies focus on explaining the mechanistic roles of the different components that lead to enhanced performance of the ternary $Cu/ZnO/ZrO_2$ catalysts. Wang et al. [35] studied the interaction of different components in the ternary Cu/ZnO/ZrO_2 (CZZ) catalyst using in-situ Diffuse Reflectance Infrared Fourier Transform Spectroscopy (DRIFTS) and DFT calculations. Although several reaction pathways involving intermediates such as the formate (HCOO), carboxyl (COOH) and CO (directly from CO_2 dissociation) are proposed in the literature [24], the DFT study of the reaction mechanism by Wang et al. [35] was restricted only to the formate pathway on the ZnO-ZrO_2 catalyst model based on their in-situ DRIFTS data which confirmed its presence on the catalyst surface. Based on the DFT and DRIFTS analyses, they proposed the reaction to proceed on the ZnO-ZrO_2 interface with hydrogen activated on the copper surface. In typical computational investigations of catalysts with multiple active sites or interfaces, the site with the strongest reactant binding energy is usually considered as the favorable site for reaction, and all further mechanistic analyses are done on that site [23,33,36]. Moreover, if one of the potential parallel pathways for methanol formation has a comparatively higher activation barrier, it is typical to neglect that particular pathway (typically the carboxyl pathway in this case) for further analyses [36,37]. Moreover, to the best of the authors' knowledge, there is no validated detailed kinetic model available for the ternary catalyst that will enable prediction of reaction behavior and optimization of operating conditions for the best yield of methanol.

Hence, this paper presents a comprehensive analysis of the methanol synthesis reaction on the $Cu/ZnO/ZrO_2$ ternary catalyst using a combination of reactor experiments, detailed DFT simulations and multi-site reactor-scale microkinetic modeling. For the mechanistic analysis using DFT simulations, a catalyst model with all three components and three active sites: the ZnO/Cu interface, the ZrO_2/Cu interface and Cu was considered. All possible reactions happening on all these sites were analyzed simultaneously to unravel the role of all three sites and all the pathways in methanol formation. Inputs from these were used to build a detailed multi-site microkinetic model which considered all three sites and a reaction network comprising all pathways on both the interfaces simultaneously which was validated against our reactor performance data, via reactor scale simulations. It is showed that this approach and the reactor scale DFT-microkinetic analyses gave different insights on the operando reaction mechanisms and the reaction progress along the packed bed reactor, compared to what was possible with the approximations mentioned earlier, which led to incomplete or misleading interpretations.

The manuscript is organized as follows. Section 2 presents the methodologies adopted in catalyst synthesis, characterization, and catalytic activity tests in the packed bed reactor, followed by the computational methods adopted in DFT modeling of the reaction network on the model ternary catalyst and the details of the multisite microkinetic modeling framework. Section 3 starts with a brief description of the catalyst characterization and is followed by the justification and rationale for the computational catalyst model adopted for the detailed DFT simulations. Next, the details pertaining to the DFT analyses of all the reaction pathways and associated energetics on different active sites are presented. This is followed by the development and validation of the detailed muti-site reactor scale microkinetic model that predicts our experimental observables such as conversion and product flow rates. Further, the reaction pathway analysis (RPA) is presented, where unique insights on the sites for reaction progress, pertinent mechanisms and how the reaction progressed along the reactor bed were obtained. This approach and analysis gave a deeper understanding of the reaction behavior that could be used for the rational design of catalysts for conducting the reaction under milder conditions.

2. Methodology

2.1. Catalyst synthesis procedure

The synthesis method and physicochemical characterization of the $Cu_2Zn_1Al_{0.7}Zr_{0.3}$ catalyst are reported in detail in our previous work [38], and it is briefly summarized here. An aqueous solution (100 cm^3, with total concentration of 1.5 M) containing appropriate amounts of Cu $(NO_3)_2$, $Al(NO_3)_3$, $Zn(NO_3)_2$ and $ZrO(NO_3)_2$ was first prepared. A second solution containing 7.15 g of Na_2CO_3 and 13.95 g of NaOH in 100 cm^3 of distilled water was then added slowly using a peristaltic pump to the former solution at room temperature under stirring to maintain the pH constant at 11. The solution was kept at 60 °C for 20 h and the resulting hydrotalcite was dried at 80 °C overnight and finally calcined at 500 °C for 4 h to obtain the catalyst.

2.2. Catalyst characterization

The chemical composition of the synthesized catalyst was determined by inductively coupled plasma atomic emission spectroscopy (ICP-AES) with a Liberty 200 spectrophotometer (Varian, Palo Alto, California, CA, USA). Samples (ca. 0.015 g) were dissolved in 2 cm^3 of a mixture of HCl (37%) and HNO_3 (70%) (3:1 by volume). After 24 h, the solutions were diluted to 250 cm^3 with Milli-Q water and analyzed.

The X-ray diffraction (XRD) analysis was performed on the fresh and the H_2-treated (5 vol% H_2 in N_2; flow rate, 15 cm^3 min^{-1} at 250 °C for 2 h) samples. XRD patterns were recorded on a X′pert Pro diffractometer (Panalytical, Malvern, UK) with θ-θ Bragg-Brentano geometry, Cu-Kα1 wavelength radiation ($\lambda = 1.5418$ Å) and X′Celerator detector, operating at 40 kV and 40 mA. The crystallite size was estimated by the Scherrer equation using the Warren correction [39].

Adsorption microcalorimetry measurements were performed with a Tian–Calvet heat flow calorimeter (Setaram, Caluire, France) equipped with a volumetric vacuum line. Each sample (ca. 0.1 g, 40–80 mesh), as prepared or previously H_2-treated (5 vol% H_2 in N_2; flow rate, 15 cm^3 min^{-1} at 250 °C for 2 h), was thermally pretreated at 220 °C for 12 h under vacuum (5×10^{-3} Pa). Adsorption was carried out by admitting successive doses of CO_2 as the probe gas at 80 °C to limit physisorption. The equilibrium pressure relative to each adsorbed amount was measured utilizing a differential pressure gauge, and the thermal effect was recorded. The run was stopped at a final equilibrium pressure of 133 Pa.

Temperature-programmed reduction (TPR) profiles were recorded with 0.030 g of catalyst on a TPD/R/O 1100 apparatus (Thermo Fisher Scientific, Waltham, Massachusetts, MA, USA) from 50° to 400°C, at 10 °C min^{-1}, under 30 cm^3 min^{-1} flow of 5 vol% H_2 in N_2. Before the experiment, samples were pretreated in nitrogen (20 cm^3 min^{-1}) at 350 °C for 2 h. The hydrogen consumption was monitored by a thermal conductivity (TCD) detector.

2.3. Catalytic activity

The performance evaluation for CO_2 hydrogenation to methanol was conducted in a customized Microactivity Efficient, PID Eng&Tech bench-scale plant, employing a high-pressure fixed bed stainless steel reactor (9.1 mm I.D. x 304.8 mm long) [40,41]. A porous plate (made of

Hastelloy C, 20 μm in size) and quartz wool were used to support the catalytic bed inside the isothermal temperature zone of the reactor. 1.0 g of calcined catalyst was diluted with α-Al_2O_3 and loaded into the reactor to obtain a total bed volume of ca. 3 cm^3. The catalyst was in-situ reduced in a stream of 15% v/v H_2/N_2 at 250 °C for 2 h under atmospheric pressure and 270 sccm flow. Upon completion of the reduction process, the reactant mixture was sent to the reactor, and the temperature varied between 200 °C and 250 °C. The catalyst activity was measured at pressures ranging from 3.0 to 7.0 MPa. Each run was held for 10 h in the same operating condition to reach a stationary catalytic behavior. The reaction stream was analyzed by a gas chromatograph (Agilent 7890B, Santa Clara, California, CA, USA) equipped with flame ionized detector (FID, for carbon-containing compounds) and thermal conductivity detector (TCD, for permanent gases), and two columns HP-Plot Q column (30 m × 0.53 mm × 40 μm) used to separate and identify CO_2, methanol, dimethyl ether, C_2 and C_3 hydrocarbons and a HP-Plot Molesieve 5 A (30 m × 0.53 mm × 50 μm) for H_2, N_2, CH_4 and CO. To avoid condensation of condensable products, connections between the plant gas outlet and GC inlet were heated at 180 °C. Nitrogen was used as an internal standard. CO_2 conversion (X_{CO_2}) and products selectivity (S_{CO}, S_{CH_3OH}, and S_{DME}), were calculated as follows:

$$X_{CO_2} = \frac{\left(\frac{CO_2}{N_2}\right)_{in} - \left(\frac{CO_2}{N_2}\right)_{out}}{\left(\frac{CO_2}{N_2}\right)_{in}} \times 100 \quad (1)$$

$$S_{CH_3OH} = \frac{\left(\frac{CH_3OH}{N_2}\right)_{out}}{\left(\frac{CO_2}{N_2}\right)_{in} - \left(\frac{CO_2}{N_2}\right)_{out}} \times 100 \quad (2)$$

$$S_{CO} = \frac{\left(\frac{CO}{N_2}\right)_{out}}{\left(\frac{CO_2}{N_2}\right)_{in} - \left(\frac{CO_2}{N_2}\right)_{out}} \times 100 \quad (3)$$

A wide range of operating conditions was covered to investigate the catalytic performance: The H_2/CO_2 molar ratio was varied between 3 and 6 mol mol^{-1}; pressures between 3.0 and 7.0 MPa; and Gas Hourly Space Velocity (GHSV) ranges between 4500 and 13,000 h^{-1}. The GHSV was calculated as follows:

$$GHSV\left(h^{-1}\right) = \frac{\text{Inlet gas } volume\left(cm^3/\text{min}\right)}{\text{Catalytic Bed Volume }\left(cm^3\right)} \bullet 60\left(\text{min}\Big/\text{h}\right) \quad (4)$$

All the catalytic studies were performed three times for each catalyst, and the values of the relative standard deviations obtained for the conversion and selectivity were in the range of 2–5%.

2.4. DFT methods

The DFT calculations were carried out using Vienna *Ab-initio* Simulation Package (VASP), version 5.4.4 [42]. The generalized gradient approximation of Perdew-Burke-Ernzerhof (PBE) [43] was employed for capturing the electronic exchange and correlation interactions. The plane wave pseudopotential implementation of DFT with kinetic energy expansion cut off 400 eV (1 eV (electron volt) = 96.4 kJ/mol), and the Projector Augmented Wave (PAW) [44] method for treatment of the core-valence electron interactions were used for all optimizations. The dispersion interactions which were not intrinsically accounted for in DFT, were incorporated using Grimme's DFT-D3 method [45].

Bulk optimization of the copper unit cell was done, and the optimized lattice constant was found to be 3.586 Å which is in close agreement with the experimental value of 3.615 Å (1 Å = 0.1 nm) [46]. Cu (111) surface was modeled with a *p4 × 5* supercell with three atomic layers consisting of 60 Cu atoms. A vacuum region of 12 Å thickness was applied to avoid interaction between the slab and its periodic images in the z direction. The bottom layer of the Cu slab was fixed during the geometry optimization to represent the bulk Cu, while the rest of the atoms were allowed to relax. The metal-metal oxide catalyst was modeled by depositing a $Zr_1Zn_2O_3$ cluster on the Cu(111) surface, representing an inverse catalyst model of metal oxide on metal. The details of this catalyst model and justification for this choice are discussed in Section 3.2. The Brillouin-zone for the *p4 × 5* supercell was sampled using 4 × 4 × 1 Monkhorst-Pack [47] k-point distribution. The minimum energy paths and the respective transition states for each of the elementary steps were estimated using the Nudged Elastic Band (NEB) method and were further refined using the Improved Dimer Method (IDM) [48] implemented in VASP. The following equations were then used to calculate the adsorption energies and the activation energy barriers of the corresponding elementary steps.

The adsorption energy of a species was calculated using the formula:

$$E_{ads} = E_{slab+species} - E_{slab} - E_{gas\ species} \quad (5)$$

where E_{ads} is the adsorption energy of the species in eV, $E_{slab+species}$ is the energy of the system where species is adsorbed on the catalyst slab in eV, E_{slab} is the energy of the pure catalyst slab in eV and $E_{gas\ species}$ is the energy of the species in the gas phase in eV.

The activation energy barrier was calculated as:

$$E_a = E_{TS} - E_r \quad (6)$$

where E_a is the activation energy barrier of the elementary reaction steps in eV, E_{TS} is the energy of the transition state complex in eV and E_r is the energy of the reactant intermediate in eV.

Geometries of all reaction intermediates and transition states were confirmed to be minima and saddle points, respectively, using vibrational frequency analysis along the reaction coordinate. The DFT calculated electronic energies were then corrected using the Zero Point Vibrational Energies (ZPVE). The free energies of the adsorption/desorption steps and elementary surface reactions were then obtained after incorporating the entropic contributions using statistical mechanics. The methodology for ZPVE and entropic corrections to the DFT potential energy are described in the Supplementary material section S.1.

2.5. Microkinetic model

A thermodynamically consistent microkinetic model was developed using data from the DFT simulations and was used to predict the bench-scale packed-bed reactor data. The reactor simulations were carried out using the Ansys CHEMKIN-PRO (2020 R1) software package [49] and an ideal steady-state isothermal plug flow reactor (PFR) model was used:

$$\frac{d(\rho u \omega_k)}{dz} = a_v W_k \sum_{i=1}^{I} \nu_{ki} r_i k \in [1, n_{gas}] \quad (7)$$

where ρ, u, ω_k and W_k are the density, the axial velocity, mass fraction of species k and the molecular weight (of species k) of the gas respectively. ν_{ki} represents the stoichiometric coefficients of species k in reaction i. r_i represents the rate of the reaction i. a_V represents the area per unit volume of the catalyst.

For surface adsorbed species,

$$\Gamma \frac{d\Theta_k}{dt} = 0 = \sum_{i=1}^{I} \nu_{ki} r_i k \in [K_{Surface}] \quad (8)$$

where Γ is the site density of the catalyst and Θ_k is the fractional site coverage of species k.

All the reactions in the microkinetic model are elementary reactions, represented as

$$\sum_{k=1}^{K} \nu'_{ki} \chi_k \leftrightarrow \sum_{k=1}^{K} \nu''_{ki} \chi_k (i = 1, 2 \ldots I) \quad (9)$$

where ν_{ki}' and ν_{ki}'' are positive integers representing stoichiometric coefficients of reactants and products, respectively; $\nu_{ki} = \nu_{ki}'-\nu_{ki}''$ is the overall stoichiometric coefficient of reaction i; and

$$r_i = k_{fi}\prod_{k=1}^{K} C_k^{\nu_{ki}'} - k_{ri}\prod_{k=1}^{K} C_k^{\nu_{ki}''} \tag{10}$$

is the rate of elementary reactions. These reaction rate constants were calculated using the Extended Arrhenius rate expression as:

$$k_f = A_i T^{\beta}\exp\left(\frac{-E_i}{RT}\right) \tag{11}$$

A_i is the pre-exponential/frequency factor, β_i is the temperature exponent, E_i is the activation energy of the ith reaction.

Fig. 1 shows the schematic of the reaction mechanism considered in this work. The final thermodynamically consistent reaction mechanism with optimized parameters is summarized in Table S4 of Supplementary material. Three different sites were considered: Cu sites where non-carbonaceous species (H#, OH#, H_2O#) can adsorb, and zinc oxide-copper (ZnO) and zirconium oxide-copper (ZrO_2) interfaces where rest of the species can adsorb. The formate (HCOO*) and carboxyl (COOH*) pathways on both ZnO/Cu and ZrO_2/Cu interfaces were explored. In the formate pathway, hydrogen is attached to the carbon of CO_2, whereas in the carboxyl pathway, hydrogen is attached to the free oxygen of adsorbed CO_2. Methanol, CO, formic acid, and water were considered as stable gas-phase products.

The activation energy and the pre-exponential factor for the individual reactions were calculated using DFT simulations and transition state theory (TST) with appropriate statistical thermodynamics expressions (details of the estimation of the pre-exponential factors are provided in Section S1 of SI). The densities of different types of active sites were calculated based on our computational catalyst model. With 14 copper atoms available on the surface of the model catalyst with an area of 128.6 Å^2, the site density of copper was $\Gamma_{Cu} = 1.81 \times 10^{-9}$ mol/cm^2. Similarly, Γ_{Zn} and Γ_{Zr} were 2.58×10^{-10} mol/cm^2 and 1.29×10^{-10} mol/cm^2, respectively.

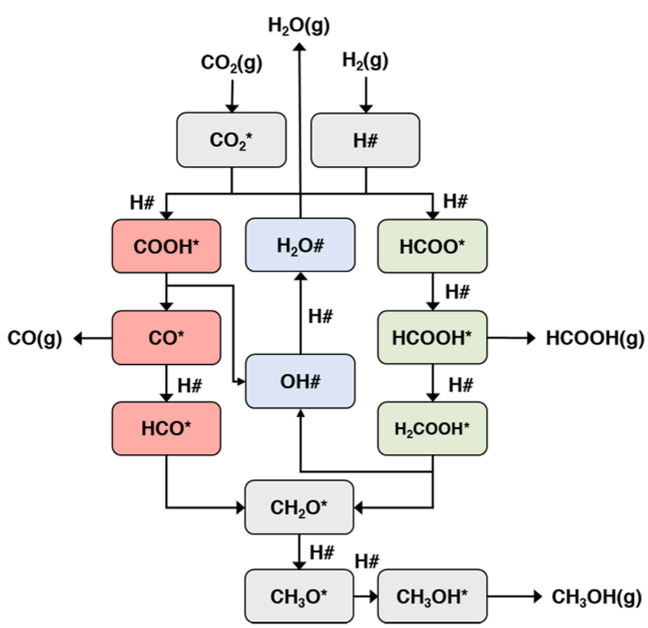

Fig. 1. The schematic of the reaction network of CO_2 hydrogenation to methanol on the Cu/ZnO/ZrO_2 catalyst. The same set of reactions were considered to take place on both ZrO_2/Cu and ZnO/Cu interfaces. '* ' (represents ZrO_2/Cu and ZnO/Cu sites) and "#" (represents pure Cu sites) indicate that the species is adsorbed on the surface. Colour codes: Green – Formate Pathway; Red – Carboxyl Pathway; Grey – Common Pathway; Blue – Water formation Pathway.

In the literature, microkinetic models are sometimes built using kinetic parameters estimated for each reaction set and in some other cases, the preliminary model is refined by optimizing the kinetic parameters of a large number of reaction sets for better prediction of experimental data [50–53]. The DFT analysis provided the set of elementary reactions in the overall mechanism as well as an initial set of kinetic parameters. Starting with the screening mechanism obtained from DFT simulations, the pre-exponential factors of four forward/backward reaction pairs were adjusted to ensure thermodynamic consistency (as discussed in Section S9.2 of SI) and improve the prediction of our lab-scale experimental data.

3. Results and discussions

3.1. Catalyst characterization

The composition of the prepared catalyst samples was analyzed using the ICP-AES technique. The experimental composition of the synthesized Cu/Zn/Zr/Al catalyst was $Cu_2Zn_{1.02}Al_{0.81}Zr_{0.25}$ and was found to be in good match against the theoretical value ($Cu_2Zn_1Al_{0.7}Zr_{0.3}$). The XRD patterns of the fresh and the reduced catalyst samples are shown in Fig. S1. XRD of the fresh catalyst showed the typical signal associated with the CuO phase, for which a mean crystallite size of 11 nm was estimated. In addition, peaks with very low intensity associated with the presence of the ZnO phase (PDF Card 75–0576) were observed, even though not clearly defined due to the superimposition with the more evident one of CuO. No peaks associated with Al_2O_3 phases were visible, probably due to its predominant amorphous character; the absence of peaks ascribable to the ZrO_2 phase can be justified accordingly. The reduced sample exhibited clear wide peaks at $2\theta =$ ca. 43.3° and 50.6° indicating the presence of face centred cubic metallic copper (Cu^0 with space group *Fm3m*) together with the presence of relatively low intensity diffraction peaks at $2\theta =$ ca. 32.4°, 36.4° and 56.9° attributed to the most intense reflection of the hexagonal zinc oxide phase (ZnO with space group *P63mc*). The TPR profiles (Fig. S2) indicated the reduction of CuO in the catalyst and the reduction of CuO to Cu is evident in the XRD pattern of the reduced catalyst.

3.2. Development and validation of the computational catalyst model

The computational catalyst model was developed based on the aforementioned information from the characterization of the $Cu_2Zn_1Al_{0.7}Zr_{0.3}$ catalyst. As TPR analysis (Fig. S2) and XRD pattern of the reduced catalyst (Fig. S1) indicated the reduction of CuO to Cu, the catalyst was modeled to contain metallic copper. XRD pattern of the reduced catalyst indicated the presence of poorly crystalline ZnO and finely dispersed ZrO_2 (no distinct peaks observed). Gao et al. [21] reported the existence of strong interactions between CuO, ZnO and ZrO_2 in Cu/ZnO/ZrO_2/Al_2O_3 catalyst prepared by a hydrotalcite method, similar to the approach adopted in this work. This was based on the absence of distinct ZnO and ZrO_2 peaks in the XRD patterns and the analyses of the X-Ray Photoelectron Spectra (XPS) of the catalyst. A similar behavior in our XRD pattern was observed and hence, direct interaction of ZnO and ZrO_2 in the catalyst was expected. Based on these inferences, the catalyst was modeled as an inverse catalyst with ZrO_x/ZnO_x deposited on metallic Cu surface. The (111) surface of Cu was chosen to represent the metallic state of Cu and a Zn_xO_y motif (x = 3 and y = 1) denoted as Zn_3O was chosen, which was found to be an approximate form of bulk wurtzite ZnO structure [54,55]. In this, a Zr atom was incorporated by substitutional replacement of one of the Zn atoms of the Zn_3O motif and two oxygen atoms were added to represent the ZrO_x/ZnO_x/Cu inverse catalyst. Hereafter the catalyst model is denoted as $Zr_1Zn_2O_3$/Cu(111) and a schematic representation of the same catalyst model is shown in Fig. S3. The zinc oxide-copper and zirconium oxide-copper interfaces at which the reaction investigations are performed will henceforth be referred to as ZnO/Cu and ZrO_2/Cu

respectively.

The validity of the features of the proposed computational catalyst model was ascertained by 1) comparison of DFT based CO_2 adsorption studies on the model catalyst against microcalorimetric measurements of CO_2 adsorption on the reduced catalyst, and 2) comparison of the computational IR spectra of key intermediates in CO_2 reduction on the catalyst model (details in Section S4.1 of SI) with operando DRIFTS data of the same species on the ternary catalyst from the literature. The differential adsorption energy (Q_{diff}) with CO_2 uptake from the microcalorimetric analysis of CO_2 loading on the reduced catalyst is shown in Fig. 2(a). The differential adsorption energy (Q_{diff}) can be obtained experimentally from the combination of the adsorption isotherm and calorimetric isotherm (integral heat of adsorption as a function of pressure), to yield the differential heat of adsorption (Q_{diff}) as a function of the number of adsorbing sites (*n*), from which it is possible to get information both on the concentration of the sites and on their strength. The CO_2 uptake at sites of different strength on the fresh and reduced catalysts are reported in Table S2. Q_{diff} values higher than 150 kJ/mol on the reduced catalyst indicated the presence of strong basic sites (refer to Section S4.2 of the SI for discussion on classification of the basic sites) which were absent in the fresh catalyst.

Systematic analysis of the adsorption energy of a single and multiple CO_2 molecules computed using DFT simulations at various interfacial sites on the $Zr_1Zn_2O_3$/Cu(111) catalyst revealed a bidentate CO_2 at the ZrO_2/Cu interface, as indicated by A in Fig. 2b to be the most favorable for single molecular adsorption. Wang et al. [35] confirmed the formation of CO_3^{2-} due to CO_2 adsorption on a Cu/ZnO/ZrO_2 catalyst from analysis of the in-situ DRIFT spectra. The adsorption energy of CO_3^{2-} species on ZnO_x/ZrO_x interface of the $Zr_1Zn_2O_3$/Cu(111) catalyst, as indicated by B in Fig. 2b was computed to be − 83 kJ/mol which was in excellent agreement with the adsorption energy from the microcalorimetry analysis during CO_2 loading. With systematic increase in the number of CO_2 molecules adsorbed on the $Zr_1Zn_2O_3$/Cu(111) catalyst (2 and 3 CO_2 molecules respectively), as indicated by C and D in Fig. 2b, the DFT computed differential adsorption energy were again in excellent agreement with the microcalorimetric analysis. Here, the DFT calculated differential adsorption energy (Q_{diff}) is defined as,

$$Q_{\text{diff}} = E_{\text{surface}+(n+1)CO_2} - E_{\text{surface}+nCO_2} - E_{CO_2(g)} \quad (12)$$

where, $E_{\text{surface}+iCO_2}$ is the energy of *i* CO_2 molecules adsorbed on the catalyst and $E_{CO_2(g)}$ is the energy of a gas-phase CO_2 molecule. These results indicate that the active site features in our model $Zr_1Zn_2O_3$/Cu (111) catalyst and the adsorption configurations of CO_2 sampled on these sites are representative of operando CO_2 adsorption on the ternary catalyst.

As an additional confirmation of the representativeness of the catalyst model, DFT computed IR frequencies of the HCOO, CH_3O and CH_3OH species which are commonly reported intermediates during CO_2 reduction on ternary Cu/ZnO/ZrO_2 catalyst [35], adsorbed at the ZrO_2/Cu and the ZnO/Cu interfaces of the $Zr_1Zn_2O_3$/Cu(111) catalyst were compared with the frequencies of the same species reported from operando DRIFTS analysis in the literature (Section S4.1 and Table S1). Good agreement between the computed and experimental frequencies of the probe species further indicates the catalyst model to have representative features of the actual catalyst.

3.3. Mechanism and reaction pathway analysis on the $Zr_1Zn_2O_3$/Cu (111) catalyst

DFT simulations of CO_2 adsorption on the $Zr_1Zn_2O_3$/Cu(111) catalyst showed strong chemisorption of CO_2 at the ZrO_2/Cu interface (−103 kJ/mol) and weaker chemisorption at the ZnO/Cu interface (−16.4 kJ/mol). Despite the huge difference in the adsorption energy of CO_2 on these two interfacial sites, both the ZrO_2/Cu and ZnO/Cu interfaces were considered as the active sites for CO_2 hydrogenation to elucidate the role of individual components of the ternary Cu/ZnO/ZrO_2 catalyst. The dissociative adsorption of H_2 on Cu(111) sites was found to be facile, with hydrogen atoms occupying the hollow sites on Cu(111) surface with an adsorption energy of − 38.9 kJ/mol. Continuous availability of the H atom near the vicinity of the ZrO_2/Cu and ZnO/Cu interfaces, where the carbonaceous species were adsorbed was assumed for the mechanistic investigation. The DFT computed reaction pathways and energy profiles on the ZrO_2/Cu and ZnO/Cu interfaces are discussed in detail in Sections 3.3.1 and 3.3.2 respectively. Based on the reaction network and the DFT computed thermodynamic and kinetic parameters, a detailed kinetic model was developed and validated against the catalytic performance data (Section 3.3.3). The validated kinetic model was used to analyze the reaction pathways and reaction rates at different zones of the catalyst bed (Section 3.3.4).

3.3.1. The mechanism on the ZrO_2/Cu interface

The free energy profile for CO_2 hydrogenation to methanol on the ZrO_2/Cu interface of the $Zr_1Zn_2O_3$/Cu(111) model that takes place through the formate and the carboxyl pathways are shown in Fig. 3a. The geometries of reaction intermediates, transition states of elementary

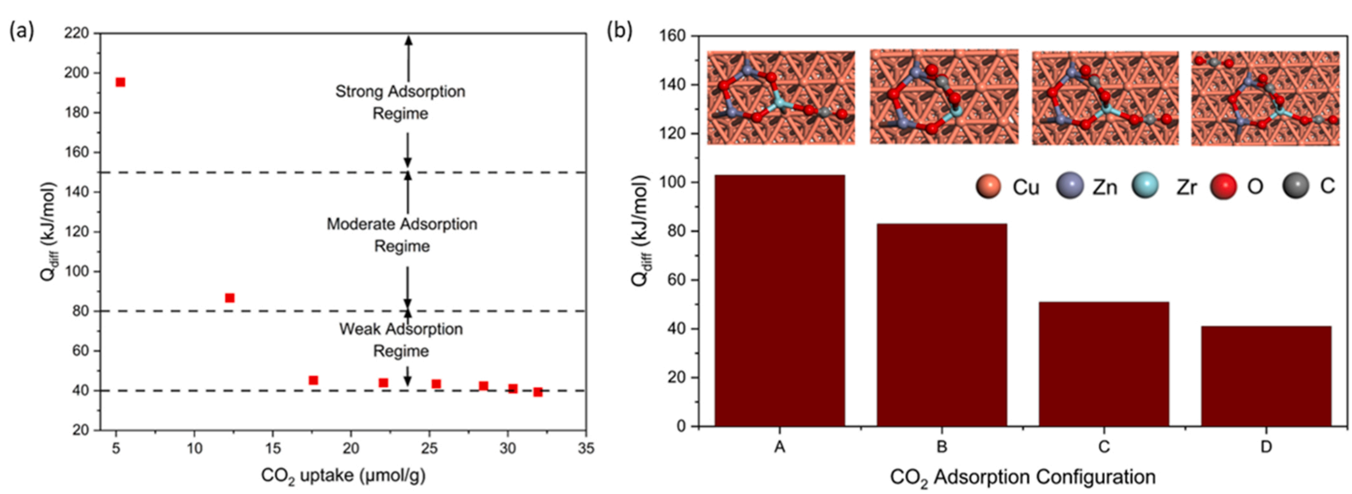

Fig. 2. (a) Differential adsorption energy (Q_{diff}) of CO_2 on reduced $Cu_2Zn_1Al_{0.7}Zr_{0.3}$ catalyst vs. CO_2 loading, obtained from microcalorimetric analysis. Red markers indicate experimental microcalorimetric analysis at different CO_2 uptake values. (b) DFT calculated differential adsorption energy of CO_2 on $Zr_1Zn_2O_3$/Cu(111) catalyst with increasing CO_2 loading. The corresponding DFT structures are: (A) CO_2 on the ZrO_2/Cu interface; (B) CO_3 on ZnO/ZrO_2; (C) CO_2 on ZrO_2/Cu with pre-adsorbed CO_3; (D) Physisorbed CO_2 with pre-adsorbed CO_2 and CO_3.

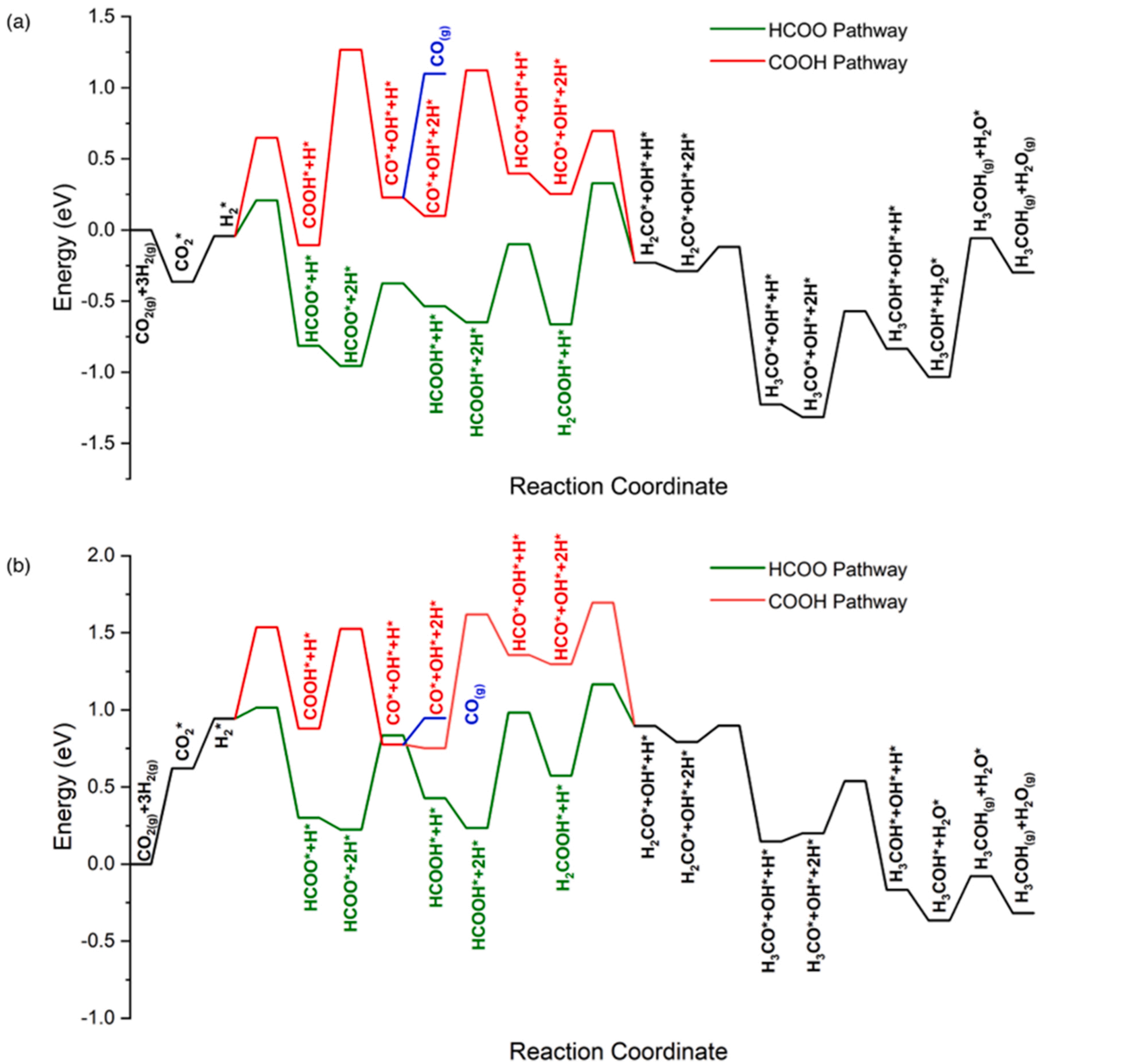

Fig. 3. Free energy profile showing different pathways for CO_2 hydrogenation to methanol on the (a) ZrO_2/Cu interface and (b) ZnO/Cu interface of the $Zr_1Zn_2O_3$/Cu (111) catalyst model obtained from DFT calculations. Green – HCOO pathway; Red – COOH pathway; Black – Common intermediates on both HCOO and COOH pathways; Blue – CO desorption in COOH pathway.

reactions and the potential energy profiles for the ZrO_2/Cu interface are provided in Figs. S4, S5, and S8 respectively. CO_2 hydrogenation initiated with the adsorption of CO_2* (ΔG_{ads}= −0.36 eV) on the interface of Zr and Cu with O and C atoms bonded to Zr and Cu atoms, respectively (Fig. S4(a)). H_2 adsorbed dissociatively on the hollow sites of Cu as 2 H* (ΔG_{ads}= 0.32 eV). CO_2* underwent hydrogenation to form either HCOO* or COOH* as the first intermediate species leading to the formate and the carboxyl pathways respectively. HCOO* was bound in a bidentate configuration with the O atoms on Zr and Cu, as shown in Fig. S4(b). Alternatively, the free O atom of CO_2* was hydrogenated to form COOH* as a bidentate species (Fig. S4(h)). Between the two steps, HCOO* formation was more exergonic (ΔG_{rxn} = −0.77 eV) than the COOH* formation (ΔG_{rxn} = −0.06 eV). The activation free energy barriers calculated for the two steps showed that the formation of HCOO* ($\Delta G^{\ddagger}$ = 0.25 eV) is kinetically more favorable than COOH* ($\Delta G^{\ddagger}$ = 0.69 eV).

HCOO* underwent hydrogenation on the oxygen to form HCOOH* (ΔG_{rxn}= 0.42 eV, $\Delta G^{\ddagger}$ = 0.58 eV) species. The formed HCOOH* species underwent further hydrogenation to H_2COOH* (ΔG_{rxn}= −0.01 eV, $\Delta G^{\ddagger}$= 0.55 eV), which was highly favorable compared to its dissociation HCO*+OH* (ΔG_{rxn}= 0.8 eV). H_2COOH* species dissociated to H_2CO*+OH* and was endergonic (ΔG_{rxn}= 0.44 eV, $\Delta G^{\ddagger}$= 0.99 eV). This was followed by further hydrogenation to form H_3CO* (ΔG_{rxn} = −0.94 eV, $\Delta G^{\ddagger}$= 0.17 eV) species. H_3CO* finally hydrogenated to H_3COH* (ΔG_{rxn}= 0.48 eV, $\Delta G^{\ddagger}$= 0.74 eV) and the remaining OH* on Cu (111) got hydrogenated to H_2O* (ΔG_{rxn} = −0.2 eV). H_3COH* and H_2O* finally desorbed with ΔG_{des} = 0.97 eV) and ΔG_{des} = −0.24 eV, respectively.

On the COOH pathway, the first intermediate COOH* dissociated to form CO* and OH* with a high activation free energy barrier of ($\Delta G^{\ddagger}$ = 1.37 eV). The CO* species formed and interacted with the ZrO_2/Cu interface while the OH species moved on to the Cu hollow site. CO* hydrogenated to HCO* (ΔG_{rxn} = 0.30 eV, $\Delta G^{\ddagger}$ = 1.02 eV) followed by its further hydrogenation to form H_2CO* (ΔG_{rxn} = −0.48 eV, $\Delta G^{\ddagger}$ =0.44 eV). H_2CO* species was the common intermediate observed for both the HCOO and COOH pathways, forming H_3COH*.

3.3.2. The mechanism on the ZnO/Cu interface

The free energy profile for CO_2 hydrogenation to methanol on the ZnO/Cu interface of the $Zr_1Zn_2O_3/Cu(111)$ catalyst model is shown in Fig. 3b. The geometries of the reaction intermediates, transition states of elementary reactions and the potential energy profiles for the ZrO_2/Cu interface are provided in Figs. S6, S7 and S9 respectively. The mechanism initiated with CO_2 adsorption on the interface of Zn and Cu with an adsorption free energy of (ΔG_{ads}= 0.62 eV). H_2 adsorbed dissociatively with an adsorption free energy of (ΔG_{ads}= 0.32 eV). The formation of HCOO* (ΔG_{rxn} = −0.64 eV, $\Delta G^{\ddagger}$ = 0.07 eV) was highly exergonic compared to formation of COOH* (ΔG_{rxn}= −0.06 eV, $\Delta G^{\ddagger}$= 0.59 eV). HCOO* hydrogenated to HCOOH* (ΔG_{rxn}= 0.20 eV, $\Delta G^{\ddagger}$= 0.61 eV), which was less favorable than on the ZrO_2/Cu interface. Unlike the exergonic HCOOH* hydrogenation to H_2COOH^* on the ZrO_2/Cu interface, it was endergonic (ΔG_{rxn}= 0.33 eV, $\Delta G^{\ddagger}$= 0.75 eV) on the ZnO/Cu interface. The H_2COOH^* species dissociated to H_2CO^* and OH* (ΔG_{rxn}= 0.32 eV, $\Delta G^{\ddagger}$= 0.59 eV) species, where the latter adsorbed at the hollow site of Cu. H_2CO^* further easily hydrogenated to H_3CO^* (ΔG_{rxn}= −0.64 eV, $\Delta G^{\ddagger}$= 0.11 eV). Finally, H_3CO^* and the remaining OH* species on the Cu surface underwent hydrogenation to H_3COH^* (ΔG_{rxn} = −0.37 eV, $\Delta G^{\ddagger}$ = 0.34 eV) and H_2O^*(ΔG_{rxn}= −0.2 eV), respectively. The desorption free energy of H_3COH^* on the ZrO_2/Cu interface was 0.97 eV, while it is significantly lower at 0.29 eV on the ZnO/Cu interface.

COOH* dissociated to CO* and OH* (ΔG_{rxn}= −0.10 eV, $\Delta G^{\ddagger}$=0.65 eV), where the former sequentially hydrogenated to form methanol. The desorption of CO* (ΔG_{des}= 0.17 eV) takes place in parallel to its hydrogenation to HCO* (ΔG_{rxn}= 0.61 eV, $\Delta G^{\ddagger}$=0.87 eV). HCO* can be hydrogenated to H_2CO^* (ΔG_{rxn}= −0.40 eV, $\Delta G^{\ddagger}$= 0.40 eV), the common intermediate observed for HCOO and COOH routes. The activation free energy barriers of the elementary steps in both formate and carboxyl pathways on the ZnO/Cu interface were lower than on the ZrO_2/Cu interface, except for formation of H_2COOH from HCOOH.

To unravel the synergetic effect of Zr in our $Zr_1Zn_2O_3/Cu(111)$ catalyst, we compared the potential energy profile of our catalyst with an existing $Zn_3O_3/Cu(111)$ (i.e., without Zr) in the literature [56]. The details presented in Section S7 of the SI show that the reaction barriers for several elementary steps are lower on our catalyst indicating a promotional effect of Zr in the catalyst.

3.3.3. Microkinetic model: Validation and species-profiles

All the reactions considered for the microkinetic model are listed in Table S4 together with the forward and backward activation energy barriers and the corresponding pre-exponential factors. The developed microkinetic model coupled with the PFR model was validated against the fixed-bed reactor experimental data and the results are shown in Figs. 4 and 5. The activity of the catalyst for CO_2 reduction to methanol was investigated in the packed-bed reactor for a range of temperatures (200–250 °C), gas-hourly space velocities (4500–13,000 h^{-1}) and inlet H_2/CO_2 ratios (See Section S8 of SI). CO_2 conversion increases with temperature and the trend was correctly captured by the microkinetic model. Fig. 4a shows the temperature dependence of overall CO_2 conversion and reactor exit CO_2 molar flowrates. Methanol synthesis from CO_2 is an exothermic reaction and reverse water-gas shift reaction, which is endothermic, takes place as a side reaction. At lower temperatures, methanol formation rates are relatively higher than CO as seen in Fig. 4b, however, the overall CO_2 conversion is low. The maximum temperature considered was limited to 250°C because a further increase in temperature would shift the thermodynamic equilibrium away from the production of methanol towards CO.

Figs. 5a and 5c show the dependence of CO_2 conversion (shown in blue symbols) on GHSV and the inlet feed composition, respectively. The corresponding model predictions are depicted using lines and solid filled columns. Whenever the reaction parameters were not varied, they were maintained at T = 250 °C, GHSV= 7000 h^{-1}, and pH_2, pCO_2, pN_2 = 19.9, 6.7, 2.9 (bar) respectively. Due to increased residence time, conversion is higher at lower GHSV as seen in Fig. 5a. It is evident from Fig. 5c that higher inlet hydrogen partial pressures give higher CO_2 conversions. Fig. 5b (symbols) and 5d (dashed columns) show the dependence of product molar flow rates on GHSV and inlet feed composition respectively obtained from the experiments. The corresponding model predictions are shown using solid lines and solid filled columns.

From Figs. 4 and 5, it is evident that the microkinetic model captured the experimental features reasonably well. The quantitative match of the DFT-microkinetic model predicted reaction performance indicators with those obtained from the bench scale reactor experiments could be attributed to the following: 1) identification and use of catalyst active site motifs representative of actual catalysts, 2) attention to ensure thermodynamic consistency in the developed microkinetic model, 3) use of appropriate computational parameters enabling minimal uncertainty in the estimated parameters, and 4) inclusion of all possible reactions across all possible sites in the microkinetic model without a priori elimination of any. More details on the thermodynamic consistency of the microkinetic model is provided in Section S9.2 of SI. The validated

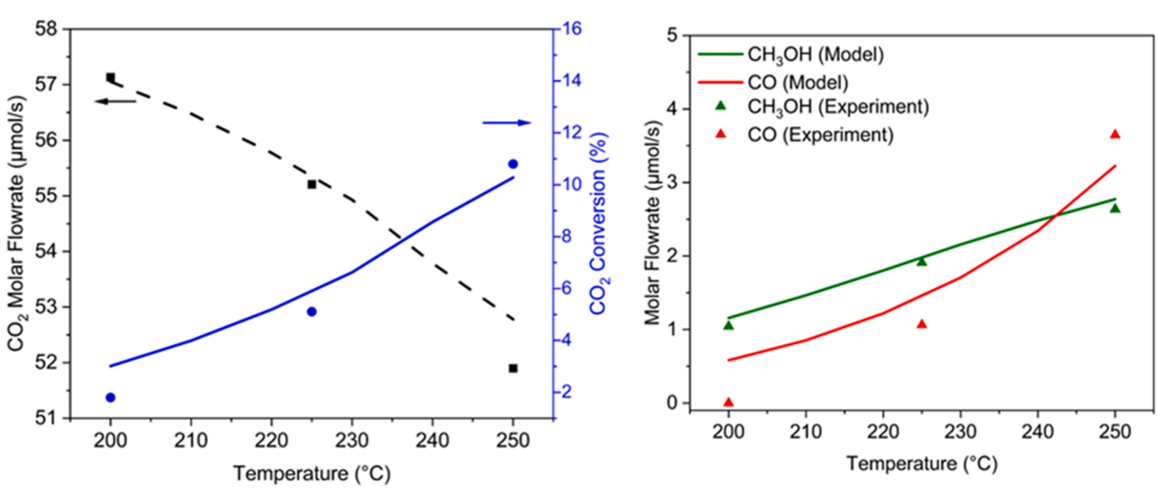

Fig. 4. CO_2 conversion (a) and product outlet molar flowrates (b) as a function of temperature. All these experiments/model data are measured/computed at P = 30 bar. T = 250 °C, GHSV= 7000 h^{-1}, inlet pH_2, pCO_2, pN_2 = 19.9, 6.7, 2.9 (bar) respectively, whenever it is not varied. Symbols represent experimental data points. Lines represent microkinetic model predicted data points. Color codes: Blue-CO_2 conversion; Black, Green, Red- reactor outlet CO_2, CH_3OH, CO molar flow rates respectively.

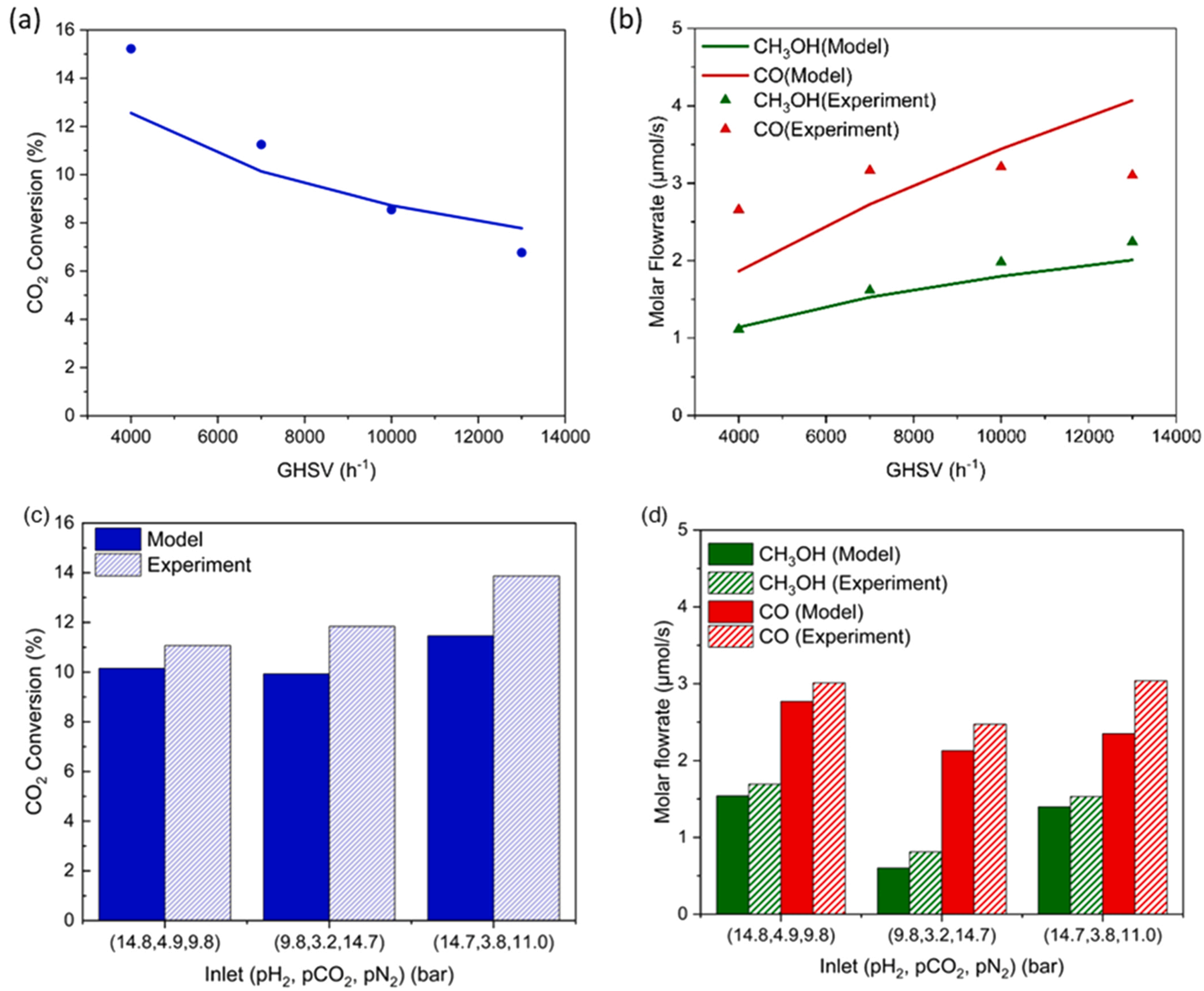

Fig. 5. CO_2 conversion, reactor outlet molar flowrates as a function of (a,b) GHSV and (c,d) feed ratios. All these experiments/model data are measured/computed at P = 30 bar. T = 250 °C, GHSV= 7000 h^{-1}, inlet pH_2, pCO_2, pN_2 = 19.9, 6.7, 2.9 (bar) respectively, whenever it is not varied. Symbols and dashed columns represent experimental data points. Lines and solid filled columns represent microkinetic model predicted data points. Color codes: Blue-CO_2 conversion; Green, Red- reactor outlet CH_3OH, CO molar flow rates respectively.

kinetic model is then used for further analysis.

The molar flow rates of unreacted gases and products along the length of the catalyst bed as predicted by the microkinetic model at T = 250 °C, GHSV= 7000 h^{-1}, inlet partial pressure, pH_2 = 19.9 bar, pCO_2 = 6.7 bar, pN_2 = 2.9 bar is shown in Fig. 6a, while the corresponding surface coverage of the reaction intermediates is shown in Fig. 6b. This is obtained as the solution of the reactor-scale microkinetic model, where the rate expressions are coupled with an ideal PFR equation (Eq. 7). As expected, there is an increase in the gas-phase concentrations of CH_3OH, CO and H_2O (scale on the right-side axis of Fig. 6(a) and a decrease in the gas-phase concentrations of CO_2 and H_2 (scale on the left-side axis of Fig. 6a) as they get consumed in the reaction. The rate of formation of methanol in the gas phase is higher near the entry of the reactor and it is in line with the behavior of surface species (Fig. 6b).

With Cu, ZrO_2/Cu interface, ZnO/Cu interface considered as active sites in the microkinetic model, the fractional site coverage of the corresponding most abundant reactive intermediates along the length of the catalyst bed are marked using different line styles: solid for Cu, dashed for ZrO_2/Cu interface and dash-dot for ZnO/Cu interface in Fig. 6b. Although H# was found to be the key adsorbed species on the Cu site, more than 80% of the Cu sites remained vacant (θ# > 0.8). Carbonaceous species were found only on the ZrO_2/Cu or ZnO/Cu interfaces. Formate (HCOO*) and methoxy (CH_3O*) were the abundant surface species on the ZrO_2/Cu interface, whereas formate (HCOO*) and methanol (CH_3OH*) dominated the ZnO/Cu interface. It is worth noting that the rate of disappearance of formate and the rate of appearance of methoxy (on ZrO_2/Cu) and methanol (on ZnO/Cu) is very high in the initial part of the bed and is explained by the reaction pathway analysis in Section 3.3.4. This also corroborates with the behavior of gas phase species where the formation of methanol is high near the entrance of the reactor. The microkinetic model predicted surface intermediates have been identified as surface species on ternary Cu/ZnO/ZrO_2 catalysts during in-situ DRIFTS analysis of CO_2 hydrogenation under similar reaction conditions in the literature [35,57], validating the computational predictions. Other surface intermediates predicted with lower coverages than these intermediates are shown in Fig. S12.

3.3.4. *Reaction pathway analysis*

As discussed in Sections 3.3.1 and 3.3.2, the reaction can either

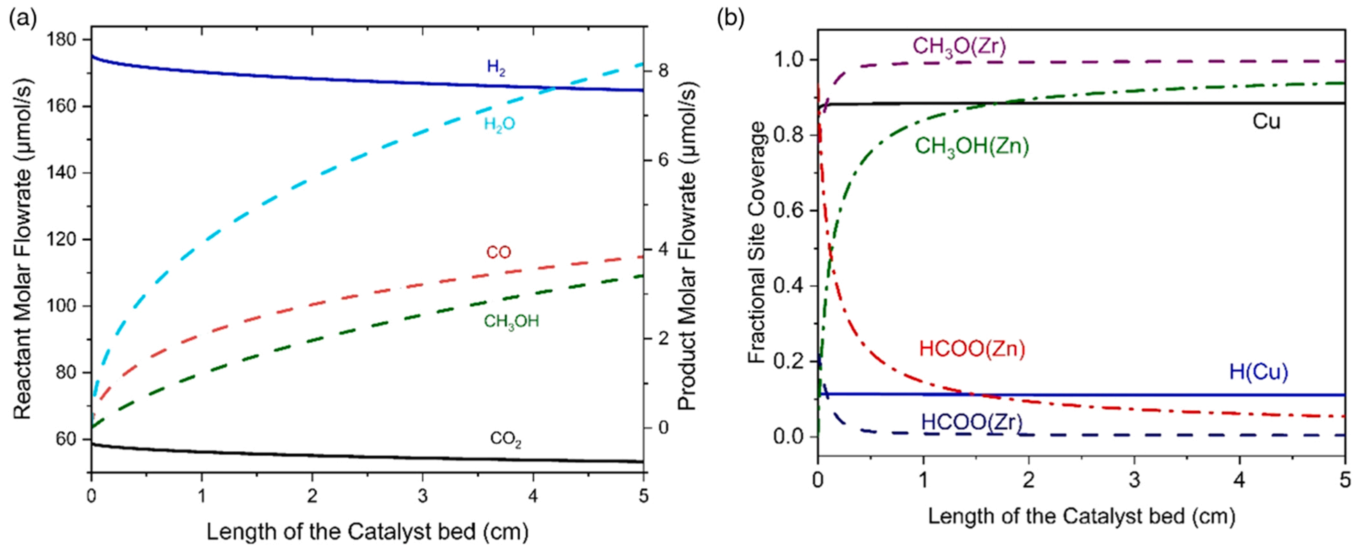

Fig. 6. (a)- The gas phase and (b) catalyst surface species as a function of catalyst bed length, obtained from the microkinetic model. In the gas-phase profile, CO_2 and H_2 have their scale on the left and the remaining species have their scale on the right. In the surface species plot, solid lines represent the species on Cu, dashed lines represent the species on ZrO_2/Cu interface and the dot-dashed lines represent the species on ZnO/Cu interface. Reaction Conditions: T = 250 °C, P = 30 bar, GHSV= 7000 h^{-1}.

proceed through the formate (right arm of Fig. 1) or the carboxyl (left arm of Fig. 1) pathways on either ZrO_2/Cu or the ZnO/Cu interfaces. The reaction pathway analysis is an outcome of our microkinetic studies and will be useful to understand the reaction behavior and hence better design the catalyst and the reactor system. The reaction pathway analysis was conducted at T = 250 °C, GHSV= 7000 h^{-1}, inlet partial pressure, pH_2 = 19.9 bar, pCO_2 = 6.7 bar, pN_2 = 2.9 bar, as a representative reaction condition. A detailed analysis of how the temperature, pressure and inlet conditions affect the reaction path analysis requires more careful attention and is skipped for brevity. The catalyst bed, which effectively is the reactor, is split into four zones for convenience of this discussion and the reaction pathway analysis is presented at all these zones: the first 0.05 cm of the reactor is attributed as zone-1; subsequent reaction pathway analyses are conducted at zone-2 (0.05–1.62 cm), zone-3 (1.63–3.31 cm) and zone-4 (3.31–5 cm) of the reactor. The reaction rate for all the elementary reactions in the complete reaction network was calculated at appropriate locations in each of the catalyst zones. Rates of selected elementary reaction steps are collected and presented in Fig. 7.

DFT-calculated CO_2 adsorption energy was lower on the ZnO/Cu interface than on the ZrO_2/Cu interface. This is corroborated by the computational CO_2 desorption simulations performed on the catalyst model in the temperature range of 300–1000 K (Section S9.4 of the SI) which also showed that ZrO_2/Cu is a strong adsorption site for CO_2 (Fig. S13). But Fig. 7a shows that the net rate of CO_2 adsorption was over nine orders of magnitude higher on the ZnO/Cu interface. This emphasizes the significance of looking at the system from a broader perspective: The adsorption energies were calculated for single adsorption steps, whereas the network of multiple reactions on different sites are coupled in a complex manner. When the microkinetic model was solved considering all the elementary reactions, the reaction prefers to primarily proceed through the ZnO/Cu interface as the activation barriers of subsequent elementary reactions are relatively lower than the ZrO_2/Cu interface.

A similar trend was observed in the rate of methanol formation, which was also higher by a similar magnitude, as the CO_2 reduction reactions primarily proceeded through the ZnO/Cu interface. This was due to the lower activation free energy barriers of CO_2 hydrogenation steps on the ZnO/Cu interface as discussed in Section 3.3.2 Additionally, the microkinetic model with only ZrO_2/Cu interface and Cu sites as the active sites present on the catalyst was simulated, unlike our original microkinetic analysis which included ZrO_2/Cu and ZnO/Cu interfaces with Cu sites. The variation of CO_2 conversion with temperatures, GHSV and inlet gas compositions, predicted by this two site microkinetic model is presented in Fig. S14. The negligible CO_2 conversion predicted by the model confirmed that the ZrO_2/Cu interface was inactive and CO_2 reduction primarily proceeded along the ZnO/Cu interface.

Since the CO_2 reduction rates on the ZnO/Cu interface are orders of magnitude higher than that on the ZrO_2/Cu interface, further reaction pathway analysis is presented only for the ZnO/Cu interface. The adsorbed CO_2 on the ZnO/Cu interface can either hydrogenate to form HCOO* or COOH* species and the DFT calculations showed lower activation free energy barriers for the formation of HCOO* . The rates of these hydrogenation reactions at different zones of the catalyst bed plotted in Fig. 7b showed the rate of formation of HCOO* is higher than the rate of formation of COOH* in Zone-1; however, the rates of HCOO* formation decline to zero (Fig. 7b) in the downstream zones. This provided a clear explanation of the behavior in Fig. 6b, where the fractional coverage of HCOO* species dropped to around 0.2 and that of CH_3OH* species increased to around 0.8 within Zone-1 of the catalyst bed. This clearly indicated that the methanol synthesis primarily takes place through the formate pathway near the reactor entrance, where the rate of methanol formation is also higher (Fig. 7a), while the carboxyl pathway is responsible for the production of methanol and CO in the downstream reactor zones.

The COOH* species dissociated on the surface to form CO* , which can either desorb (CO formation via RWGS) or further hydrogenate to form methanol through the direct CO hydrogenation pathway via HCO* intermediate. The rates of formation of CO gas and the formation of HCO* by CO hydrogenation, plotted in Fig. 7c showed that CO desorption is the likely reaction in Zone-1. The rate of CO desorption gradually decreased along the length of the catalyst bed, while the rate of hydrogenation remained nearly invariant. The higher rate of CO desorption near the inlet of the reactor is also reflected in the higher molar flowrate of CO in the initial catalyst zone (Fig. 6a) and the gradually flattening along the catalyst length. Based on the preferential hydrogenation of CO* to form HCO* in the subsequent reactor zones, one can infer that both CO_2 and CO hydrogenation are both important “global” steps for methanol synthesis.

Since CH_2O* is a common intermediate for both the formate and the

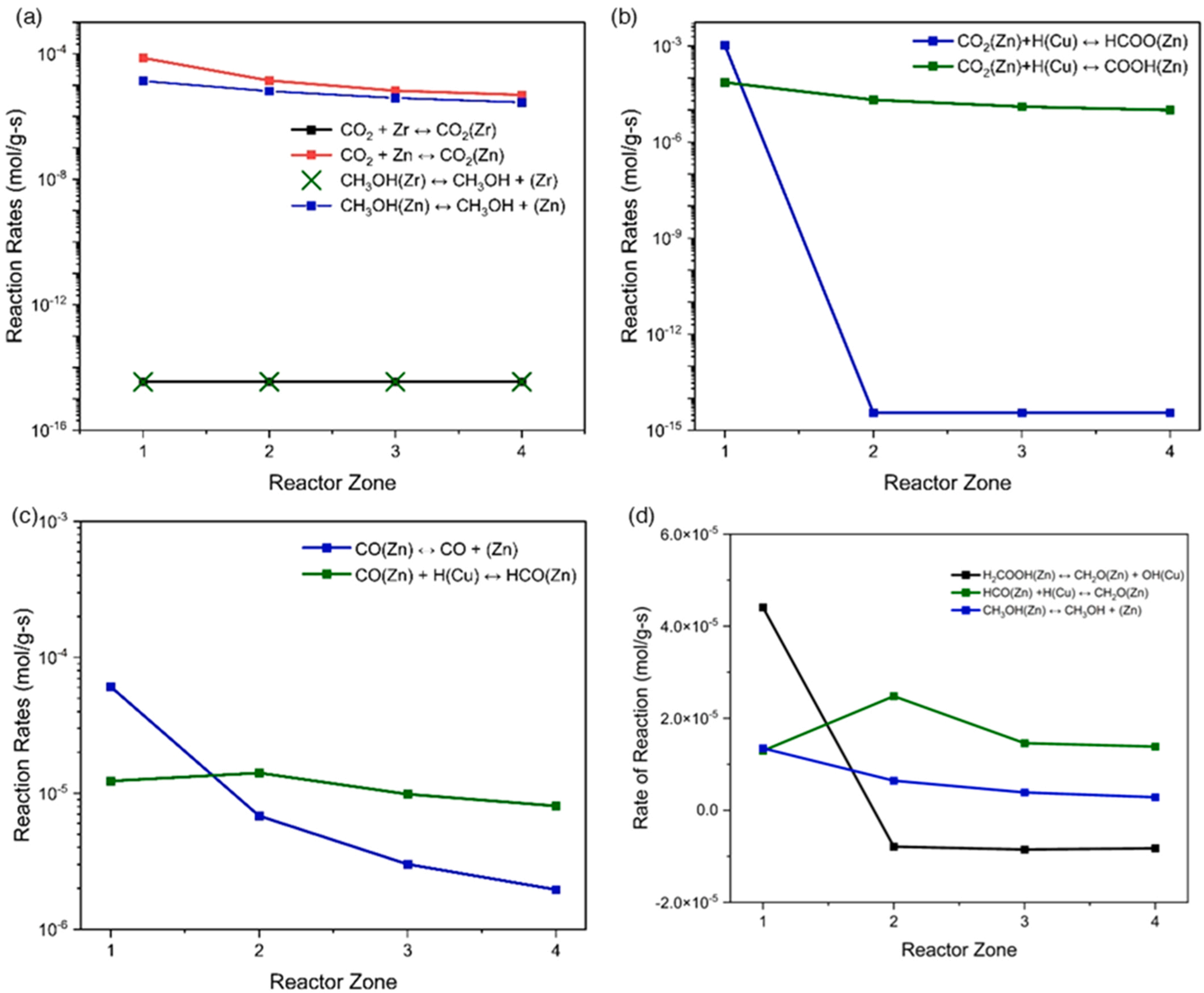

Fig. 7. Comparison of various elementary reaction rates calculated using the microkinetic model (a) CO_2 adsorption rates on ZrO_2/Cu interface and ZnO/Cu interface (b) CO_2 hydrogenation rates on the ZnO/Cu interface to produce HCOO* and COOH* (c) CO desorption and hydrogenation rates on the ZnO/Cu interface (d) The contribution of the formate and carboxyl pathway towards methanol synthesis on the ZnO/Cu interface. Reaction Conditions: T = 250 °C, P = 30 bar, GHSV= 7000 h^{-1}. It is to be noted that the ordinates of (a), (b), (c) are log-scale and (d) has a linear-scale.

carboxyl pathway (see Fig. 1), the rate of formation of CH_2O^* in each of these pathways is another quantitative metric to ascertain the pathway towards methanol formation. Fig. 7d presents the rate of formation of CH_2O^* from H_2COOH^* (formate pathway) and from HCO* (carboxyl pathway). CH_2O^* is involved in the following three reactions (with the corresponding forward and reverse activation energy barriers in in kJ/mol in curly brackets):

(i) $H_2COOH(Zn) + V(Cu) \leftrightarrow CH_2O(Zn) + OH(Cu)$ [Formate Pathway] {77.04, 28.51}
(ii) $HCO(Zn) + H(Cu) \leftrightarrow CH_2O(Zn) + V(Cu)$ [Carboxyl Pathway] {35.7, 66.59}
(iii) $CH_2O(Zn) + H(Cu) \leftrightarrow CH_3O(Zn) + V(Cu)$ [Common Pathway] {5.46, 51.38}

Reaction (iii) is kinetically most favorable followed by (ii). Thus, when the surface concentration of CH_2O^* increases, the carboxyl pathway dominates in all the reaction zones except in Zone-1. Also shown in the figure is the rate of methanol desorption which almost mimics the trend in the rate of formation of CH_2O^* from HCO* . Fig. 7d confirms the inferences in the previous discussions, where the formate pathway contributes towards methanol production in the initial zone of the reactor while the carboxyl pathway almost exclusively contributes towards methanol formation in the later zones. Furthermore, methanol desorption rates corroborate with the gas-phase concentration profile of methanol, where the initial slope is higher, and it gets flatter in the later parts of the reactor.

4. Conclusions

A combination of reactor experiments, detailed DFT simulations of a complex reaction network and a multi-site first-principles microkinetic model were used to understand the mechanistic behavior of the methanol synthesis reaction and to elucidate the role of individual components of the $Cu_2Zn_1Al_{0.7}Zr_{0.3}$ catalyst.

The $Cu_2Zn_1Al_{0.7}Zr_{0.3}$ catalyst was synthesized by the coprecipitation method and characterized for the structural features using XRD and TPR techniques. The XRD analysis of the reduced catalyst showed the reduction of CuO to a metallic Cu, with weakly crystalline ZnO and finely dispersed ZrO_2, indicative of strong interaction between all the

catalyst components. The catalytic performance of the ternary catalyst was evaluated in a fixed bed reactor at varying conditions of reaction temperature, reactor pressure, inlet flowrate and composition of the gases.

A computationally tractable catalyst model representative of the inverse catalyst, with active site features validated against microcalorimetric measurements of CO_2 uptake and in-situ DRIFTS analysis of CO_2 hydrogenation was used for detailed mechanistic analysis using DFT simulations. The ZrO_2/Cu interface on the ternary catalyst was identified as the strong CO_2 adsorption site while metallic copper served as the active hydrogen supply site.

A mean-field multi-site reactor-scale microkinetic model based on DFT calculations on the ternary $Cu_2Zn_1Al_{0.7}Zr_{0.3}$ catalyst was developed and found to predict the catalytic performance and product flow rate well. Despite the ZrO_2/Cu interface being a strong adsorption site for CO_2, the microkinetic results showed that the ZnO/Cu interface is the crucial reaction center at the desired reaction conditions (T-200–250 °C, P-30 bar). The reaction progressed many orders of magnitude faster on the ZnO/Cu interface due to the relatively "moderate" CO_2 binding energy and comparatively lower activation free energy barriers for surface reactions than at the ZrO_2/Cu interface. The lowering of barrier on the ZnO/Cu interface appears to be due to the synergistic effect of the ZrO_2 incorporation. Hence, it is hypothesized that the promotional effect of Zr in the ternary catalyst is both indirect as suggested in the literature and mechanistic as revealed from this investigation. The reaction pathway analyses predicted methanol formation via both the formate and the carboxyl pathways to be relevant. The formate pathway was prevalent in the initial part of the reactor while the carboxyl pathway was dominant in the later part. HCOO* and CH_3OH* were found to be the most abundant reaction intermediates on the ZnO/Cu interface during the reaction.

Unique insights into the reaction behavior at different parts of the reactor were unraveled due to the multi-site reaction network considerations in the modeling framework, without a priori elimination of reaction pathways. Multistage validations of the computational catalyst model and reaction mechanisms, and thermodynamic consistency analysis enabled development of a first principles detailed kinetic model for the ternary catalyst capable of predicting catalytic performance and product profiles at desired conditions. Microkinetic analysis provides insights into catalyst structure-activity correlations which can effectively be used in rational design of advanced catalytic materials. Insights into the reaction behavior along the reactor enables identification of strategies for optimization and design of appropriate reactors.

CRediT authorship contribution statement

Balaji C Dharmalingam: Investigation, Formal analysis and writing original draft. **Ajay Koushik V:** Formal analysis, Investigation, Writing - original draft. **Mauro Mureddu:** Investigation, writing-original draft. **Luciano Atzori:** Investigaiton. **Sarah Lai:** Investigaiton. **Alberto Pettinau:** Funding acquisition, Supervision. **Niket S. Kaisare:** Conceptualization, Supervision, Writing - review & editing. **Preeti Aghalayam:** Conceptualization, Supervision, Writing - review & editing. **Jithin John Varghese:** Conceptualization, Funding acquisition, Supervision, Writing - review & editing.

Declaration of Competing Interest

The authors declare that they have no known competing financial interests or personal relationships that could have appeared to influence the work reported in this paper.

Data Availability

Data will be made available on request.

Acknowledgement

BCD, AKV, NSK, PA and JJV acknowledge the Carbon Capture Utilization and Storage (CCUS) laboratory, IIT Madras for the facilities. The authors acknowledge the use of the High-Performance Computing Environment (HPCE), IIT Madras for the computing resources for the DFT calculations. JJV acknowledges the New Faculty Seed Grant (CHE/19–20/713/NFSC/JITH) from IIT Madras. The experimental part of this study has been performed by SOTACARBO within the Advanced Sustainable technologieS for Energy Transition, ASSET project (CUP D43C22002400002), funded by the Regional Government of Sardinia.

Appendix A. Supporting information

Supplementary data associated with this article can be found in the online version at doi:10.1016/j.apcatb.2023.122743.

References

[1] J. Blunden, State of the climate in 2020, Bull. Am. Meteorol. Soc. 102 (2020) S1–S475, https://doi.org/10.1175/2021BAMSStateoftheClimate.1.
[2] IPCC, Global warming of 1.5°C: IPCC special report on impacts of global warming of 1.5°C above pre-industrial levels in context of strengthening response to climate change. Sustainable Development, and Efforts to Eradicate Poverty, Cambridge University Press, 2022, https://doi.org/10.1017/9781009157940.
[3] T. Sakakura, J.C. Choi, H. Yasuda, Transformation of carbon dioxide, Chem. Rev. 107 (2007) 2365–2387, https://doi.org/10.1021/cr068357u.
[4] I. Dimitriou, P. García-Gutiérrez, R.H. Elder, R.M. Cuéllar-Franca, A. Azapagic, R. W.K. Allen, Carbon dioxide utilisation for production of transport fuels: process and economic analysis, Energy Environ. Sci. 8 (2015) 1775–1789, https://doi.org/10.1039/c4ee04117h.
[5] K. Li, J.G. Chen, CO_2 hydrogenation to methanol over ZrO_2-containing catalysts: insights into ZrO_2 induced synergy, ACS Catal. 9 (2019) 7840–7861, https://doi.org/10.1021/acscatal.9b01943.
[6] F. Zeng, C. Mebrahtu, X. Xi, L. Liao, J. Ren, J. Xie, H.J. Heeres, R. Palkovits, Catalysts design for higher alcohols synthesis by CO_2 hydrogenation: trends and future perspectives, Appl. Catal. B. 291 (2021), 120073, https://doi.org/10.1016/j.apcatb.2021.120073.
[7] M. Behrens, F. Studt, I. Kasatkin, S. Kühl, M. Hävecker, F. Abild-Pedersen, S. Zander, F. Girgsdies, P. Kurr, B.-L. Kniep, M. Tovar, R.W. Fischer, J.K. Nørskov, R. Schlögl, The active site of methanol synthesis over Cu/ZnO/Al_2O_3 industrial catalysts, Science 336 (2012) 893–897, https://doi.org/10.1126/science.1219831.
[8] O. Martin, A.J. Martín, C. Mondelli, S. Mitchell, T.F. Segawa, R. Hauert, C. Drouilly, D. Curulla-Ferré, J. Pérez-Ramírez, Indium oxide as a superior catalyst for methanol synthesis by CO_2 hydrogenation, Angew. Chem., Int. Ed. Engl. 55 (2016) 6261–6265, https://doi.org/10.1002/anie.201600943.
[9] M. Mureddu, F. Ferrara, A. Pettinau, Highly efficient CuO/ZnO/ZrO_2@SBA-15 nanocatalysts for methanol synthesis from the catalytic hydrogenation of CO_2, Appl. Catal. B. 258 (2019), 117941, https://doi.org/10.1016/j.apcatb.2019.117941.
[10] X. Hu, C. Zhao, Q. Guan, X. Hu, W. Li, J. Chen, Selective hydrogenation of CO_2 over a Ce promoted Cu-based catalyst confined by SBA-15, Inorg. Chem. Front. 6 (2019) 1799–1812, https://doi.org/10.1039/c9qi00397e.
[11] S. Li, L. Guo, T. Ishihara, Hydrogenation of CO_2 to methanol over Cu/AlCeO catalyst, Catal. Today 339 (2020) 352–361, https://doi.org/10.1016/j.cattod.2019.01.015.
[12] M. Zabilskiy, K. Ma, A. Beck, J.A. Van Bokhoven, Methanol synthesis over Cu/CeO_2-ZrO_2 catalysts: the key role of multiple active components, Catal. Sci. Technol. 11 (2021) 349–358, https://doi.org/10.1039/d0cy01762k.
[13] W. Wang, Z. Qu, L. Song, Q. Fu, CO_2 hydrogenation to methanol over Cu/CeO_2 and Cu/ZrO_2 catalysts: Tuning methanol selectivity via metal-support interaction, J., Energy Chem. 40 (2020) 22–30, https://doi.org/10.1016/j.jechem.2019.03.001.
[14] F. Arena, K. Barbera, G. Italiano, G. Bonura, L. Spadaro, F. Frusteri, Synthesis, characterization and activity pattern of Cu-ZnO/ZrO_2 catalysts in the hydrogenation of carbon dioxide to methanol, J. Catal. 249 (2007) 185–194, https://doi.org/10.1016/j.jcat.2007.04.003.
[15] T. Witoon, N. Kachaban, W. Donphai, P. Kidkhunthod, K. Faungnawakij, M. Chareonpanich, J. Limtrakul, Tuning of catalytic CO_2 hydrogenation by changing composition of CuO-ZnO-ZrO_2 catalysts, Energy Convers. Manag. 118 (2016) 21–31, https://doi.org/10.1016/j.enconman.2016.03.075.
[16] G. Bonura, M. Cordaro, C. Cannilla, F. Arena, F. Frusteri, The changing nature of the active site of Cu-Zn-Zr catalysts for the CO_2 hydrogenation reaction to methanol, Appl. Catal. B. 152–153 (2014) 152–161, https://doi.org/10.1016/j.apcatb.2014.01.035.
[17] E. Frei, A. Schaadt, T. Ludwig, H. Hillebrecht, I. Krossing, The influence of the precipitation/ageing temperature on a Cu/ZnO/ZrO_2 catalyst for methanol synthesis from H_2 and CO_2, ChemCatChem 6 (2014) 1721–1730, https://doi.org/10.1002/cctc.201300665.
[18] M.Z. Ramli, S.S.A. Syed-Hassan, A. Hadi, Performance of Cu-Zn-Al-Zr catalyst prepared by ultrasonic spray precipitation technique in the synthesis of methanol

via CO_2 hydrogenation, Fuel Process. Technol. 169 (2018) 191–198, https://doi.org/10.1016/j.fuproc.2017.10.004.
[19] P. Gao, R. Xie, H. Wang, L. Zhong, L. Xia, Z. Zhang, W. Wei, Y. Sun, Cu/Zn/Al/Zr catalysts via phase-pure hydrotalcite-like compounds for methanol synthesis from carbon dioxide, J. CO_2 Util. 11 (2015) 41–48, https://doi.org/10.1016/j.jcou.2014.12.008.
[20] Y. Zhang, L. Zhong, H. Wang, P. Gao, X. Li, S. Xiao, G. Ding, W. Wei, Y. Sun, Catalytic performance of spray-dried Cu/ZnO/Al2O3/ZrO2 catalysts for slurry methanol synthesis from CO_2 hydrogenation, J. CO_2 Util. 15 (2016) 72–82, https://doi.org/10.1016/j.jcou.2016.01.005.
[21] P. Gao, F. Li, H. Zhan, N. Zhao, F. Xiao, W. Wei, L. Zhong, H. Wang, Y. Sun, Influence of Zr on the performance of Cu/Zn/Al/Zr catalysts via hydrotalcite-like precursors for CO_2 hydrogenation to methanol, J. Catal. 298 (2013) 51–60, https://doi.org/10.1016/j.jcat.2012.10.030.
[22] A. Arandia, J. Yim, H. Warraich, E. Leppäkangas, R. Bes, A. Lempelto, L. Gell, H. Jiang, K. Meinander, T. Viinikainen, S. Huotari, K. Honkala, R.L. Puurunen, Effect of atomic layer deposited zinc promoter on the activity of copper-on-zirconia catalysts in the hydrogenation of carbon dioxide to methanol, Appl. Catal. B. 321 (2023), https://doi.org/10.1016/j.apcatb.2022.122046.
[23] L. Gell, A. Lempelto, T. Kiljunen, K. Honkala, Influence of a Cu-zirconia interface structure on CO_2 adsorption and activation, J. Chem. Phys. 154 (2021), 214707, https://doi.org/10.1063/5.0049293.
[24] S. Kattel, P. Liu, J.G. Chen, Tuning selectivity of CO_2 hydrogenation reactions at the metal/oxide interface, J. Am. Chem. Soc. 139 (2017) 9739–9754, https://doi.org/10.1021/jacs.7b05362.
[25] S. Kattel, B. Yan, Y. Yang, J.G. Chen, P. Liu, Optimizing binding energies of key intermediates for CO_2 hydrogenation to methanol over oxide-supported copper, J. Am. Chem. Soc. 138 (2016) 12440–12450, https://doi.org/10.1021/jacs.6b05791.
[26] P. Gao, F. Li, N. Zhao, F. Xiao, W. Wei, L. Zhong, Y. Sun, Influence of modifier (Mn, La, Ce, Zr and Y) on the performance of Cu/Zn/Al catalysts via hydrotalcite-like precursors for CO_2 hydrogenation to methanol, Appl. Catal. A. 468 (2013) 442–452, https://doi.org/10.1016/j.apcata.2013.09.026.
[27] H. Li, L. Wang, X. Gao, F.S. Xiao, Cu/ZnO/Al_2O_3 catalyst modulated by zirconia with enhanced performance in CO_2 hydrogenation to methanol, Ind. Eng. Chem. Res. 61 (2022) 10446–10454, https://doi.org/10.1021/acs.iecr.2c00172.
[28] Q.L. Tang, W.T. Zou, R.K. Huang, Q. Wang, X.X. Duan, Effect of the components' interface on the synthesis of methanol over Cu/ZnO from CO_2/H_2: a microkinetic analysis based on DFT + U calculations, Phys. Chem. Chem. Phys. 17 (2015) 7317–7333, https://doi.org/10.1039/c4cp05518g.
[29] K. Mondal, Megha, A. Banerjee, A. Fortunelli, M. Walter, M. Moseler, Ab initio modeling of the ZnO-Cu(111) interface, J. Phys. Chem. C. 126 (2022) 764–771, https://doi.org/10.1021/acs.jpcc.1c09170.
[30] S. Polierer, J. Jelic, S. Pitter, F. Studt, On the reactivity of the Cu/ZrO_2 system for the hydrogenation of CO_2 to methanol: a density functional theory study, J. Phys. Chem. C. 123 (2019) 26904–26911, https://doi.org/10.1021/acs.jpcc.9b06500.
[31] C. Wu, L. Lin, J. Liu, J. Zhang, F. Zhang, T. Zhou, N. Rui, S. Yao, Y. Deng, F. Yang, W. Xu, J. Luo, Y. Zhao, B. Yan, X.D. Wen, J.A. Rodriguez, D. Ma, Inverse ZrO_2/Cu as a highly efficient methanol synthesis catalyst from CO_2 hydrogenation, Nat. Commun. 11 (2020) 5767, https://doi.org/10.1038/s41467-020-19634-8.
[32] J. Wang, G. Li, Z. Li, C. Tang, Z. Feng, H. An, H. Liu, T. Liu, C. Li, A highly selective and stable ZnO-ZrO_2 solid solution catalyst for CO_2 hydrogenation to methanol, Sci. Adv. 3 (2017), https://doi.org/10.1126/sciadv.1701290.
[33] K. Larmier, W.C. Liao, S. Tada, E. Lam, R. Verel, A. Bansode, A. Urakawa, A. Comas-Vives, C. Copéret, CO_2-to-methanol hydrogenation on zirconia-supported copper nanoparticles: reaction intermediates and the role of the metal–support, Interface, Angew. Chem., Int. Ed. Engl. 56 (2017) 2318–2323, https://doi.org/10.1002/anie.201610166.
[34] S. Kattel, P.J. Ramírez, J.G. Chen, J.A. Rodriguez, P. Liu, Active sites for CO_2 hydrogenation to methanol on Cu/ZnO catalysts, Science 355 (2017) 1296–1299, https://doi.org/10.1126/science.aal3573.
[35] Y. Wang, S. Kattel, W. Gao, K. Li, P. Liu, J.G. Chen, H. Wang, Exploring the ternary interactions in Cu–ZnO–ZrO_2 catalysts for efficient CO_2 hydrogenation to methanol, Nat. Commun. 10 (2019) 1166, https://doi.org/10.1038/s41467-019-09072-6.
[36] H. Chen, H. Cui, Y. Lv, P. Liu, F. Hao, W. Xiong, H. Luo, CO_2 hydrogenation to methanol over Cu/ZnO/ZrO_2 catalysts: effects of ZnO morphology and oxygen vacancy, Fuel 314 (2022), 123035, https://doi.org/10.1016/j.fuel.2021.123035.
[37] D. Kopač, B. Likozar, M. Huš, Catalysis of material surface defects: Multiscale modeling of methanol synthesis by CO_2 reduction on copper, Appl. Surf. Sci. 497 (2019), 143783, https://doi.org/10.1016/j.apsusc.2019.143783.
[38] M. Mureddu, S. Lai, L. Atzori, E. Rombi, F. Ferrara, A. Pettinau, M.G. Cutrufello, Ex-ldh-based catalysts for CO_2 conversion to methanol and dimethyl ether, Catalysts 11 (2021) 615, https://doi.org/10.3390/catal11050615.
[39] H.P. Klug, L.E. Alexander. X-Ray Diffraction Procedures: For Polycrystalline and Amorphous Materials, second ed., Wiley-Interscince Publications, 1974.
[40] A. Pettinau, M. Mureddu, F. Ferrara, Carbon dioxide conversion into liquid fuels by hydrogenation and photoelectrochemical reduction: project description and preliminary experimental results, Energy Procedia 114 (2017) 6893–6904, https://doi.org/10.1016/j.egypro.2017.03.1832.
[41] G. Lombardelli, M. Mureddu, S. Lai, F. Ferrara, A. Pettinau, L. Atzori, A. Conversano, M. Gatti, CO_2 hydrogenation to methanol with an innovative Cu/Zn/Al/Zr catalyst: Experimental tests and process modeling, J. CO_2 Util. 65 (2022), 102240, https://doi.org/10.1016/j.jcou.2022.102240.
[42] G. Kresse, J. Furthmüller, Efficient iterative schemes for ab initio total-energy calculations using a plane-wave basis set, Phys. Rev. B Condens. Matter Mater. Phys. 54 (1996) 11169–11186, https://doi.org/10.1103/PhysRevB.54.11169.
[43] J.P. Perdew, K. Burke, M. Ernzerhof, Generalized gradient approximation made simple, Phys. Rev. Lett. 77 (1996) 3865–3868, https://doi.org/10.1103/PhysRevLett.77.3865.
[44] D. Joubert, From ultrasoft pseudopotentials to the projector augmented-wave method, Phys. Rev. B Condens. Matter Mater. Phys. 59 (1999) 1758–1775, https://doi.org/10.1103/PhysRevB.59.1758.
[45] A. Allouche, Software news and updates gabedit — a graphical user interface for computational chemistry softwares, J. Comput. Chem. 32 (2012) 174–182, https://doi.org/10.1002/jcc.
[46] M.E. Straumanis, L.S. Yu, Lattice parameters, densities, expansion coefficients and perfection of structure of Cu and of Cu–In α phase, Acta Crystallogr. A. 25 (1969) 676–682, https://doi.org/10.1107/S0567739469001549.
[47] H.J. Monkhorst, J.D. Pack, Special points for Brillouin-zone integrations, Phys. Rev. B 13 (1976) 5188–5192, https://doi.org/10.1103/PhysRevB.13.5188.
[48] A. Heyden, A.T. Bell, F.J. Keil, Efficient methods for finding transition states in chemical reactions: comparison of improved dimer method and partitioned rational function optimization method, J. Chem. Phys. 123 (2005), 224101, https://doi.org/10.1063/1.2104507.
[49] M.E. Coltrin, R.J. Kee, F.M. Rupley, Surface chemkin: a general formalism and software for analyzing heterogeneous chemical kinetics at a gas-surface interface, Int. J. Chem. Kinet. 23 (1991) 1111–1128, https://doi.org/10.1002/kin.550231205.
[50] L.C. Grabow, M. Mavrikakis, Mechanism of methanol synthesis on Cu through CO_2 and CO hydrogenation, ACS Catal. 1 (2011) 365–384, https://doi.org/10.1021/cs200055d.
[51] J. Park, J. Cho, Y. Lee, M.J. Park, W.B. Lee, Practical microkinetic modeling approach for methanol synthesis from syngas over a Cu-based catalyst, Ind. Eng. Chem. Res. 58 (2019) 8663–8673, https://doi.org/10.1021/acs.iecr.9b01254.
[52] A.K. Raghu, N.S. Kaisare, Microkinetic modeling and analysis of CO_2 methanation on ruthenium, Ind. Eng. Chem. Res. 59 (2020) 16161–16169, https://doi.org/10.1021/acs.iecr.0c02685.
[53] D. Schmider, L. Maier, O. Deutschmann, Reaction kinetics of CO and CO_2 methanation over nickel, Ind. Eng. Chem. Res. 60 (2021) 5792–5805, https://doi.org/10.1021/acs.iecr.1c00389.
[54] T. Reichenbach, K. Mondal, M. Jäger, T. Vent-Schmidt, D. Himmel, V. Dybbert, A. Bruix, I. Krossing, M. Walter, M. Moseler, Ab initio study of CO_2 hydrogenation mechanisms on inverse ZnO/Cu catalysts, J. Catal. 360 (2018) 168–174, https://doi.org/10.1016/j.jcat.2018.01.035.
[55] T. Lunkenbein, J. Schumann, M. Behrens, R. Schlögl, M.G. Willinger, Formation of a ZnO overlayer in industrial Cu/ZnO/Al_2O_3 catalysts induced by strong metal-support interactions, Angew. Chem. Int. Ed. Engl. 54 (2015) 4544–4548, https://doi.org/10.1002/anie.201411581.
[56] M. Huš, D. Kopač, N.S. Štefančič, D.L. Jurković, V.D.B.C. Dasireddy, B. Likozar, Unravelling the mechanisms of CO_2 hydrogenation to methanol on Cu-based catalysts using first-principles multiscale modelling and experiments, Catal. Sci. Technol. 7 (2017) 5900–5913, https://doi.org/10.1039/c7cy01659j.
[57] F.C.F. Marcos, F.M. Cavalcanti, D.D. Petrolini, L. Lin, L.E. Betancourt, S. D. Senanayake, J.A. Rodriguez, J.M. Assaf, R. Giudici, E.M. Assaf, Effect of operating parameters on H_2/CO_2 conversion to methanol over Cu-Zn oxide supported on ZrO_2 polymorph catalysts: characterization and kinetics, Chem. Eng. J. 427 (2022), 130947, https://doi.org/10.1016/j.cej.2021.130947.